Correction of CCI cloud data over the Swiss Alps using ground-based radiation measurements

Fanny Jeanneret [1], Giovanni Martucci [2], Simon Pinnock [1], and Alexis Berne [3]

[1]ESA ECSAT, Harwell Campus, Didcot, Oxfordshire, OX11 0FD, United Kingdom
[2]Federal Office of Meteorology and Climatology MeteoSwiss, Ch. de l'Aérologie, Payerne, Switzerland
[3]EPFL, EPFL-ENAC-IIE-LTE, Lausanne, Switzerland

Correspondence to: Fanny Jeanneret (Fanny.Jeanneret@meteoswiss.ch)

Abstract. The validation of long term cloud datasets retrieved from satellites is challenging due to their worldwide coverage going back as far as the 1980s. A trustworthy reference cannot be found easily at every location and every time. Mountainous regions present a particular problem since ground-based measurements are sparse. Moreover, as retrievals from passive satellite radiometers are difficult in winter due to the presence of snow on the ground, it is particularly important to develop new ways to evaluate and to correct satellite datasets over elevated areas.

In winter for ground levels above 1000m (a.s.l.) in Switzerland, the cloud occurrence of the newly-released cloud property datasets of the ESA Climate Change Initiative Cloud_cci project (AVHRR-PM and MODIS-Aqua series) is 132 % to 217 % that of SYNOP observations, corresponding to between 24 % and 54 % of false cloud detections. Furthermore, the overestimations increase with the altitude of the sites and are associated with particular retrieved cloud properties.

In this study, a novel post-processing approach is proposed to reduce the amount of false cloud detections in the satellite datasets. A combination of ground-based downwelling longwave and shortwave radiation and temperature measurements is used to provide independent validation of the cloud cover over 41 locations in Switzerland. An agreement of 85 % is obtained when the cloud cover is compared to surface synoptic observations (90 % within $\pm$ 1 okta difference). The validation data is then co-located with the satellite observations and a decision tree model is trained to automatically detect the overestimations in the satellite cloud masks. Cross-validated results show that 62 ± 13 % of these overestimations can be identified by the model, reducing the systematic error in the satellite datasets from 14.4 ± 15.5 % to 4.3 ± 2.8 %. The amount of errors is lower, and importantly, their distribution is more homogeneous as well. These corrections happen at the cost of a global increase of 7 ± 2 % of missed clouds. Using this model, it is possible to significantly improve the cloud detection reliability in elevated areas in the Cloud_cci's AVHRR-PM and MODIS-Aqua products.

1 Introduction

Clouds have a major importance in climate: they play a key role in the radiation budget (Trenberth, 2009) and the water cycle, which then impact almost every component of the climatic system. As the climate changes, cloud properties change as well (Quaas, 2015; Norris et al., 2016; Davies et al., 2017). Detecting and analysing these changes is only possible with high quality datasets spanning several decades. Satellite instruments are the most suitable tools for the global observation of clouds,

and scientific effort is increasingly focusing on reprocessing historical records to extract as much information as possible from them. In 2010, the European Space Agency started the Climate Change Initiative (CCI) programme (Hollmann et al., 2013) to coordinate scientific work towards the production, homogenisation and validation of long-term datasets constructed from different satellite instruments. The CCI project dedicated to clouds, the Cloud_cci (Stengel et al., 2015), is releasing

5   its open datasets at the time of writing of this paper. Two of them are of particular interest here: the dataset based on the Advanced Very High Resolution Radiometer afternoon series (AVHRR-PM), and the dataset based on MODerate-resolution Imaging Spectroradiometer (MODIS) Aqua data. AVHRR-PM has a long time coverage, which gives the opportunity to look for climate change signals. The MODIS-Aqua dataset is processed by the Cloud_cci using the same algorithm (CC4CL, Sus et al., 2018; McGarragh et al., 2018) as AVHRR-PM, only with a higher spatial resolution.

10   In mountainous regions, processes such as elevation-dependent warming (Rangwala and Miller, 2012; Pepin et al., 2015) are documented, suggesting climate might change faster with increasing altitude. Thus, signs of climate change should be easier to observe in elevated areas, either due to larger amplitudes or to earlier appearance. However, mountains are one of the most challenging places for satellite measurements: the accuracy of geolocation is lower over complex terrain, and radiometers measurements often lack sufficient information to clearly discriminate between snow and clouds (Musial et al., 2014). As a

15   consequence, datasets based only on satellite radiometers have a lower quality in winter in mountainous areas, and this study proposes a way of addressing this limitation by combining ground-based information and machine learning techniques.

Ground-based data have long been used to estimate cloud cover, for instance synoptic observations (Barbaro et al., 1981), passive measurements of shortwave (Pagès et al., 2003; Long et al., 2006; Martínez-Chico et al., 2011), longwave (Dürr and Philipona, 2004; Herrmann et al., 2015) and microwave radiation, as well as active instruments such as cloud radars and lidars.

20   The latter ones can indisputably provide accurate measurements of cloud properties like occurrence, altitude and lifetime, but due to their cost they are quite rare and often do not have long historical records. This study hence combines measurements of downwelling longwave and shortwave radiation to detect cloud occurrence at 41 locations in Switzerland. This new ground-based cloud information (henceforth referred to as a "cloud mask") covers the period from 1995 to the end of 2014, with different lengths (6.1 ± 4.8 years on average) at different locations, and is validated against synoptic observations for 24 of the

25   41 stations.

Once the ground-based cloud mask is computed from the radiation data, it is used as reference to train an automated algorithm to detect false cloud measurements in the satellite pixels at the 41 locations. A brief analysis of the types of situations inducing the retrieval algorithm errors is conducted. Time series of cloud properties are also presented, as well as the impact of the removal of points identified as false clouds by the model trained in this study. Then, after investigating the possibilities for

30   spatial extrapolation, the algorithm is applied to every satellite pixel in a defined area to identify false clouds *when* and *where* no information about the true cloud cover is available. As the focus of this study is on mountainous areas, the geographical zone of interest covers the Swiss Alps. The time frame is 1982-2012 for the AVHRR-PM dataset, and 2002-2014 for MODIS-Aqua.

2 Satellite data in the Alps

In this section, an overview of the problems encountered when using two datasets of the Cloud_cci in mountainous regions is presented. The characteristics and limitations of the two datasets are summarised, and cloud occurrences in the European Alps are shown as example. A local validation test is made using 24 ground-based stations in Switzerland, and shows that when
5   snow is present in the retrieval pixel, cloud amounts are significantly overestimated.

2.1 CCI datasets

Two open datasets of the Cloud_cci are used: the first one is derived from the AVHRR instruments (Cracknell, 1997) onboard 7 satellites of the US National Oceanic and Atmospheric Administration (NOAA). The second dataset is from the MODIS instrument (Barnes et al., 1998) onboard Aqua, one of the A-Train satellites of the US National Aeronautics and Space Admin-
10 istration (NASA). These instruments are passive spectroradiometers measuring top-of-atmosphere radiances at five channels, the so-called AVHRR-heritage channels, centred approximately at 0.6, 0.8, 3.7, 11, and 12 μm. AVHRR on NOAA-16 had a different setup: a 1.6 μm-channel was used in daytime instead of the 3.7 μm-channel, until this was changed to the same setup as the others in May 2003. For consistency with AVHRR-based datasets, the Cloud_cci MODIS datasets are based on MODIS-Aqua measurements made at these five wavelengths even though the instrument measures at 36 different channels in
15 total.

The level 3U (corresponding to level 2 uncollated data mapped onto a spatial grid), version 002 of the datasets was used (DOIs can be found in the references, under Stengel et al. (2017b) and Stengel et al. (2017c)). The AVHRR-PM dataset covers the years 1982-2012 and has a resolution of 0.05 lat/lon degrees; MODIS-Aqua spans from 2002 to 2012 and is mapped onto a 0.02 lat/lon degrees grid over Europe. All instruments are on polar-orbiting sun-synchronous satellites and overpass locally
20 in early afternoon (around 13:00) and early morning (around 01:00). Since the orbits of the NOAA satellites were allowed to drift, the local time of each AVHRR observation also drifts by several hours over the lifetime of each satellite (Heidinger et al., 2014).

Cloud properties are retrieved from the satellite-measured radiances using an optimal estimation approach, following the theoretical basis for inverse retrieval methods described in Rodgers (2004). The algorithm, called Community Cloud retrieval
25 for Climate (CC4CL), works in three steps: first, a neural network trained on co-located data from CALIPSO-CALIOP (Winker et al., 2009) is run on the measured radiances to determine if a cloud is present or not. Then, the cloud phase is determined with a decision tree, as proposed by Pavolonis and Heidinger (2004) and Pavolonis et al. (2005). Lastly, the retrieval is done using the measured radiances and some ancillary data such as atmospheric pressure, temperature and ozone, snow and ice cover, and land and sea surface temperature, all coming from ECMWF ERA Interim (Dee et al., 2011), along with surface reflectance
30 from the MODIS MCD43C1 product (Schaaf et al., 2010). The cloud top pressure, cloud optical thickness and cloud effective radius are returned directly by the optimal estimation, whereas the cloud top height, cloud top temperature, cloud albedo, liquid and ice water path are then inferred from them. For more information, the algorithm is described in detail in Sus et al. (2018) and McGarragh et al. (2018).

As detailed in Stengel et al. (2017a), one of the particularities of these datasets is that they include uncertainty estimates at all processing levels. Validation of the Cloud_cci datasets is described in Stapelberg et al. (2017), but as it was done for the whole Earth, topographic details are not necessarily taken into account. In that report, false alarm rates above 25 % are often seen to occur during daytime above polar snow- and ice-covered surfaces, which might be observed above high-elevated areas as well. When compared to CALIPSO-CALIOP (a satellite lidar instrument), more than 50 % of clouds under 0.15 optical thickness in CALIOP dataset is missing in AVHRR-PM and MODIS-Aqua datasets. Comparison of cloud occurrences with SYNOP observations (described in the next section) show a good agreement of the seasonal cycles, but overestimations (5 to 10 %) during winter in the Northern hemisphere, particularly mid-latitudes in Europe and Asia.

2.2 Visual observations

Surface synoptic (SYNOP) observations are done every 3, 6 or 12 hours at manned meteorological stations: an observer looks at the sky, mentally separating it in an 8-slice pie of which they would be the centre. For each of the eight sky slices, the observer determines if clouds are present, and if so, estimates their type and altitude. The cloud coverage is hence evaluated in numbers from 0 to 8 called oktas, with an extra value 9 for totally obscured sky (by fog or other meteorological phenomena; these values were discarded). 24 stations in Switzerland are used in this study (a detailed list with operational times can be found in Appendix Table A1). The exact observation time is not available, but spans between 11.45 and 12.00 UTC.

To ease the comparison with the satellite's binary cloud masks, a limit was set at 0-3 oktas for clear skies and 4-8 oktas for cloudy skies, which means that only significant amounts of reported clouds will be categorised as cloudy conditions. It is consistent with the different viewing geometries involved, since the human observer might see much further than the satellite pixel's limits when the cloud cover is relatively sparse. Other thresholds were tested, and confirmed that a 3-oktas threshold is an optimal compromise between classifying too many and not enough situations as cloudy. This value is further confirmed by Bojanowski et al. (2014), which use the same threshold.

As the satellites overpass in early afternoon, their observations can be matched to SYNOP observations done at 12 UTC at the 24 stations in Switzerland. At every location, the SYNOP observations are compared with the satellite data falling in the corresponding pixel (approximately 1x1 km^2 for MODIS-Aqua and 4x4 km^2 for AVHRR-PM) between 11.40 and 12.20 UTC. The uncertainty of the comparisons are unknown, since SYNOP observations are not provided with uncertainties. The satellite cloud masks do not have associated data quality flags either. For SYNOP observations, known sources of uncertainties are: the subjectivity of human observations and their inevitable variation from one observer to another (Mittermaier, 2012); the scenery effect (Malberg, 1973; Karlsson, 2003; Werkmeister et al., 2015) which increases the difficulty of comparing two different observation geometries, as cloud fractional cover tends to be overestimated by a ground-based observer looking in a slanted way at clouds spread vertically, especially when clouds are low on the horizon; and the detection difference between a human eye limited to the visible spectra and satellite sensors, which have wider spectral ranges, especially infrared wavelengths.
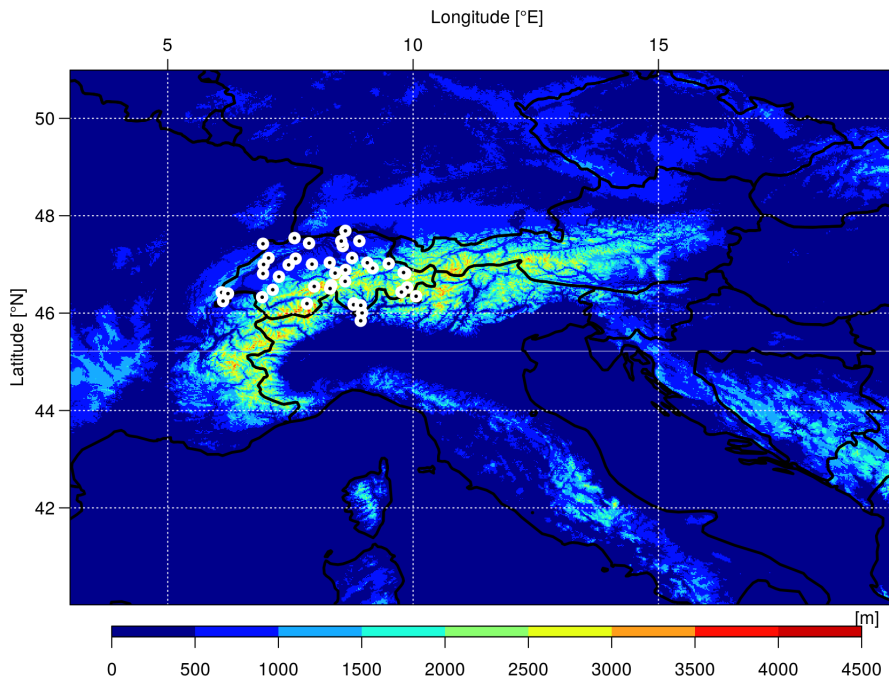
Figure 1. Geographical area considered in this study, with ground elevation represented by colors and ground-based stations by white dots.

2.3   Satellite cloud mask

A geographical area centred in the Alps was defined as area of interest for this study: it spans from 40 to 51 °N and from 3 to 20 °E (Fig. 1). In this area, the MODIS dataset's cloud mask was averaged by season, and winter and summer averages are presented in Fig. 2. As can be observed, mountain reliefs are systematically associated with an increase in cloud occurrence,
5   especially in winter. The same pattern is observed when averaging the cloud mask of the AVHRR-PM dataset, but cannot be found in ERA-Interim cloud mask data (not shown).

   The increase of cloud cover with altitude is confirmed independently of the instrument or of the time period considered (Fig. 3). There is a slightly different relationship between ground altitude and cloud occurrence in the two datasets due to their different spatial resolution. In very high areas, the cloud cover is constantly overestimated (it often reaches values larger than
10   80 % of cloud occurrence) regardless of the season, whereas in lowlands the values found are more consistent and lower in summer than in winter, which is also observed in a satellite and ground-based instruments intercomparison by Fontana et al. (2013)

   In Figure 3, different clusters of points can be observed in winter (two clusters) and in summer (three): they are caused by natural variations of cloud amounts with latitude. The low-occurrence group of points in winter (Fig. 3a,c,e) corresponds to
15   cloud occurrences of satellite pixels above sea and above lowlands south of the Alps (approximately below 46° N) whilst the high-occurrence group contains pixels north of the Massif Central in France, of the Alps and of the Dinaric Alps in Eastern
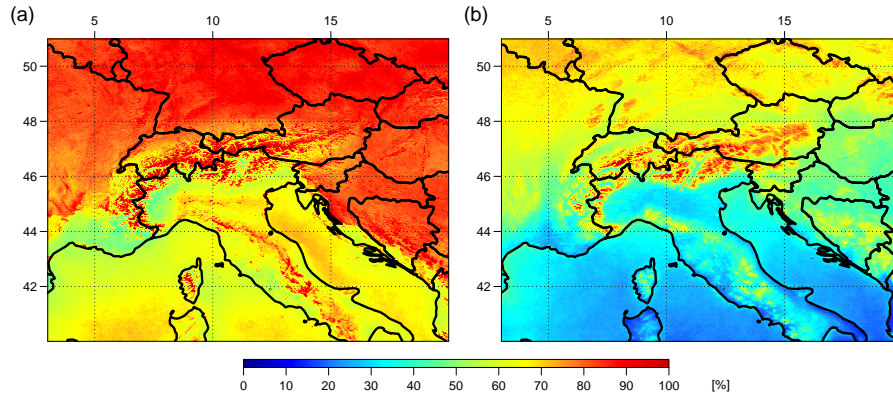
Figure 2. Winter (Dec., Jan., Feb.) (a) and summer (June, July, Aug.) (b) averaged cloud occurrences in MODIS-Aqua L3U dataset, years 2003-2014.
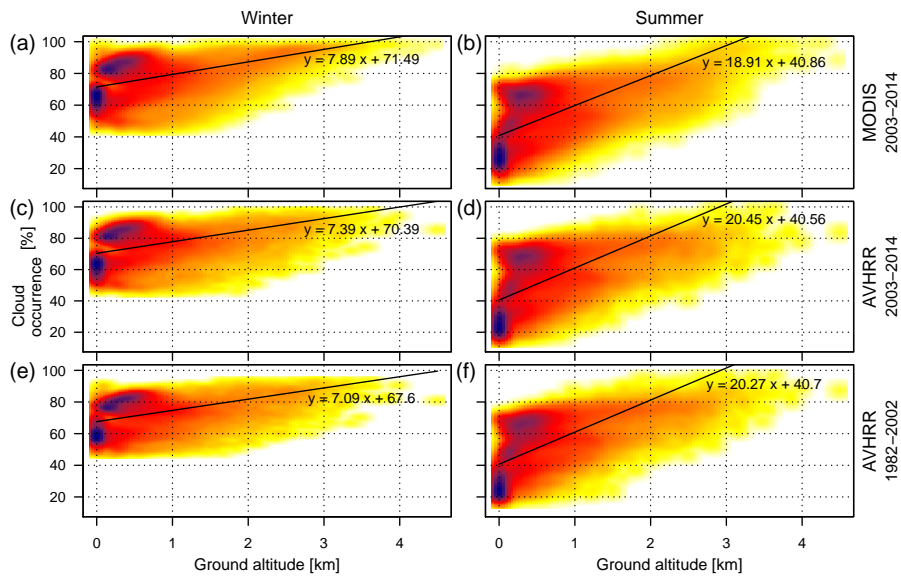

Figure 3. Winter (left) and summer (right) cloud occurrences for each pixel in the Alps (area shown in Fig. 2), for MODIS-Aqua 2003-2014 (a and b), AVHRR-PM 2003-2014 (c and d) and the first part of the AVHRR-PM record (1982-2002, e and f). Colours indicate the density of points (the darker it is, the more points there are). A linear regression is drawn and written on each subfigure to illustrate the overall observed relationship between ground altitude and cloud occurence.

Europe. In summer (Fig. 3b,d,f), cloud amounts get lower and three groups can be identified: the lower one, as in winter, corresponds to pixels above sea or south of the Alps; the middle one contains pixels above lowlands between roughly 46 and 48° N (between the Massif Central and the Alps, and between the Alps and the Dinaric Alps), and the upper group is above lowlands north of the Alps (over 48° N). Winter retrievals of AVHRR-PM 2003-2014 (Fig. 3c) have lower cloud occurrences
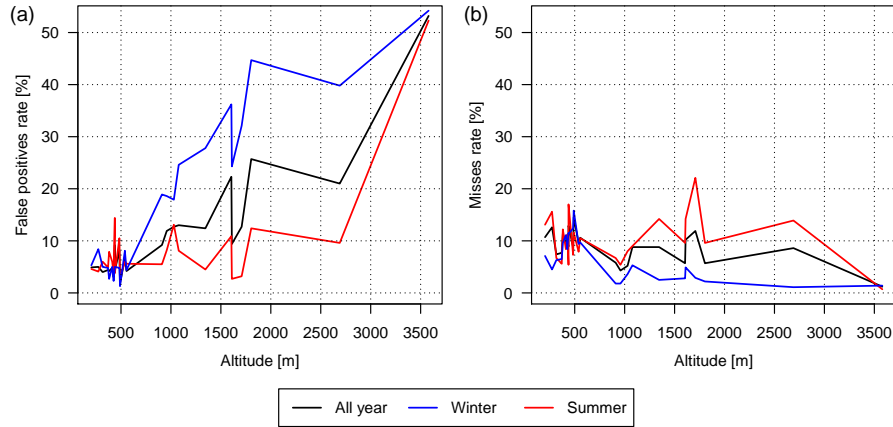
Figure 4. MODIS-Aqua cloud mask compared to 24 SYNOP stations in Switzerland. The SYNOP-MODIS overlaps varies from one station to another, from 3.3 years to the whole MODIS record (12 years). The satellite mask false positives (a) correspond to when the satellite dataset contains a cloud, but the ground observer reports a value of less than 4 oktas of clouds. The misses (b) are the opposite disagreement between the two.

(approx. -3%) than those of AVHRR-PM 1982-2002 (Fig. 3e). As discussed later, the satellite's orbital drift might have had an impact on the values.

When comparing the cloud mask of MODIS-Aqua to SYNOP observations (Fig. 4), extreme values are seen at the Jungfraujoch station (3580m above sea level), where clouds are reported 98 % of the time in the satellites datasets, corresponding to
5   53 % of false positives. This rate (Fig. 4a) indeed increases with altitude, more drastically in winter and consistently with the spatial pattern observed before. Night satellite measurements are not exempt from these overestimations, although fewer SYNOP data are available as reference (elevated stations are not manned at night). The decrease of the misses rate with altitude (Fig. 4b), especially in winter, is directly related to the high overestimation rate at these locations. Except for that, the misses rate observed is relatively steady with altitude. It shows a systematic bias of 5-10 %, most likely caused by the different ge-
10   ometries involved in the comparison. For instance, ground observers might see much further than the boundary of the satellite pixel in which they stand, especially in locations without surrounding relief blocking the view. Considering also the limitations detailed in Subsection 2.2, the cloud masks are overall considered as agreeing under 1000m.

These results suggest that the presence of snow on the ground, in winter and in summer in high-altitude locations, tricks the satellite retrieval algorithm into detecting more clouds than it should. This is consistent with the Appendix of Stengel
15   et al. (2017a), which mentions that the known limitations of these satellite datasets include "*shortcomings in cloud detection and optical property retrievals in regions with high surface reflection of solar radiation*". Snow reflectance leads to top-of-atmosphere radiances very similar to water and/or ice clouds in different channels. Some methods can be used to help distinguish between them (see for instance Musial et al. (2014)). A widely used solution is to complement spectral data with ancillary data: CC4CL, the retrieval producing the satellite datasets shown here, is indeed based on the snow mask of ERA-
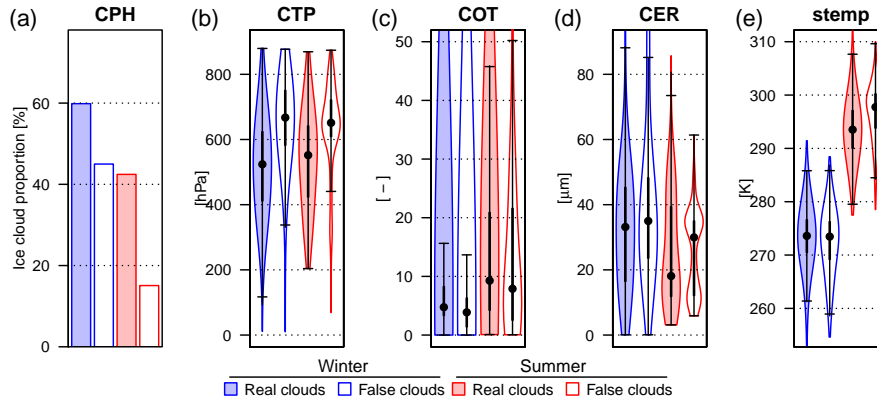
Figure 5. Distributions of values of five cloud properties (phase (CPH), top pressure (CTP), optical thickness (COT), effective radius (CER), surface temperature (stemp)) retrieved from MODIS-Aqua in winter and summer at 9 stations located above 1000m of altitude, for actual clouds and falsely detected ones (using SYNOP observations as reference).

Interim. However, given the issues observed here, the spatial resolution (0.7 °lat/lon in ERA-Interim, much lower than that of the satellite products: MODIS-Aqua is 0.02 °lat/lon and AVHRR 0.05 °lat/lon), the quality or the use of the ancillary data might be insufficient.

2.4 Satellite cloud properties

As the cloud property retrieval from satellite-measured radiances is run after the cloud mask computation by the artificial neural networks, any mistake at this first stage carries on to the next. Attempting to retrieve cloud properties in the absence of cloud would lead to unreasonable values. For instance, false clouds are more often of liquid phase than ice (Fig. 5a), are significantly closer to the ground (higher top pressure, 5b), have lower cloud optical thickness but higher cloud effective radius (5c and d), and have higher surface temperatures (5e). A surprisingly high mode can also be seen in the effective radius distribution (5d) of false clouds in summer, corresponding supposedly to ice particles. These observations are consistent with a retrieval influenced by the presence of snow: these false clouds are lower, warmer and with larger particles than actual clouds. In summary, cloud mask errors have an important impact on the retrieved cloud properties as well, and identifying such cases before any in-depth analysis is very important.

3 Radiation cloud mask

The previous section presented briefly how the CC4CL satellite retrieval overestimates cloud amounts above elevated areas. The next two sections propose a solution to handle this issue: first, a new binary cloud mask is defined. The combination of several ground-based observations provides insight about the cloud cover at 41 locations in Switzerland. This allows the use of a larger amount of locations than the SYNOP stations, especially with more data in elevated areas and without potential issues

regarding the subjectivity of SYNOP observations. Subsequently, this cloud mask is used as reference to train a model for the automated detection of false clouds in the satellite datasets.

3.1 Ground-based data

Downwelling longwave and shortwave radiation as well as ground-based 2-metre air temperatures are used in this study to
5   get an estimation of the local cloud cover. Longwave and shortwave downwelling radiation is measured by pyrgeometers and pyranometers, respectively, which consist in a thermopile sensor and a temperature sensor under a small dome. The pyrgeometer's spectral band is 4.5 - 42 μm, whereas the pyranometer's is 0.3 - 3 μm. Both instruments have a field of view close to an ideal 180 degrees (the exact values depend on the instrument's quality), and each measurement is weighted by the cosine of the incidence angle, giving more importance to radiation at angles close to the zenith.

10   All measurements were converted to 10-minute averages. Information about the measurement setup and data preprocessing can be found in the work by Dürr and Philipona (2004). Of the 41 stations used in this study, 37 are part of the SwissMetNet network (Suter et al., 2006) operated by the Swiss weather office MeteoSwiss, and 4 are part of the Alpine Surface Radiation Budget (ASBR) network (Marty et al., 2002). The pyrgeometers used in the SwissMetNet network are of type CG4 and CGR4 from Kipp & Zonen, with a declared uncertainty of 3 %. Older measurements from the ASRB network have been taken by
15   modified Eppley PIR pyrgeometer, which have an observed uncertainty of 3 Wm^{-2} (Marty et al., 2002). The pyranometers are mostly CM21 from Kipp & Zonen (2 % uncertainty) and a few SPN1 from Delta-T (5 % or 10 Wm^{-2}). A detailed list of stations including operation times can be found in Appendix Table A1.

3.2 Topographic data

Topographic information comes from the freely available Global Digital Elevation Model (GDEM) ASTER version 2 (Tachikawa
20   et al. (2011); ASTER GDEM is a product of METI and NASA). This GDEM has a spatial resolution of 1 arc-second (approximately 30 metres at the equator).

3.3 Method for the ground-based cloud mask

The method described here combines two different types of radiation to estimate the state of the sky at 41 locations, with a 10-minute temporal resolution.

25   Ground-based longwave measurements have been used in various ways to estimate cloud cover (e.g., Dürr and Philipona, 2004; Dupont et al., 2008; Viúdez-Mora et al., 2009). The method used here is inspired by the work of Herrmann et al. (2015) and consists in converting downwelling longwave measurements (L, Wm^{-2}) into estimated sky temperatures (T_{sky}, K), then comparing them to ground-based (2 metres) temperatures. As the radiation emitted by a cloud is comparable to that of a black body at the same temperature, Stefan-Boltzmann law is used for the conversion:

30    $$T_{\mathrm{sky}} = (\frac{L}{\epsilon\sigma})^{\frac{1}{4}} ,\tag{1}$$

where σ is Stefan-Boltzmann constant ($5.67 \cdot 10^{-8}$ $\mathrm{Wm}^{-2}\mathrm{K}^{-4}$) and the atmospheric emissivity ϵ is approximated to unity.
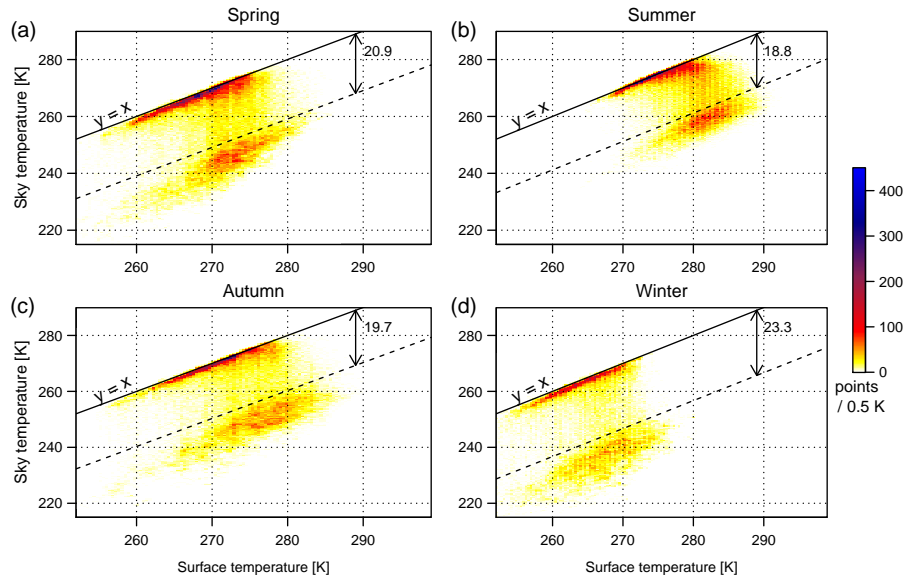
Figure 6. Comparison of daytime sky and ground temperatures at Weissfluhjoch station (2690m) in Switzerland, per season, using data from 1994 to 2010. The upper cluster corresponds to in-cloud and overcast conditions, whilst the lower one corresponds to clear-sky times. The points in-between are partially cloudy conditions. The dashed line corresponds to the automatically detected threshold under which values are considered as being part of the lower cluster.

Figure 6 shows cluster plots of the estimated sky temperature versus the measured ground temperature. Clear sky estimates always cluster at low temperatures (being a mixture of atmospheric and cosmic background temperatures), whereas cloud base temperatures are significantly higher (representative of tropospheric temperatures at the cloud height). Scattered cloud conditions are characterised by values falling between the two main clusters.

5   The detection of the lower cluster border is done in five steps. First, the differences between ground and sky temperatures are calculated. Then, the density distribution of these values is computed (black curve in Fig. 7) and smoothed (red curve). One way to find the cluster border is to look for a strong density increase in this distribution, so in the third step, the derivative (blue curve in Fig. 7) is computed. As the upper cluster is spread over several kelvin degrees, only temperature differences larger than 5 K can correspond to the lower cluster. The fourth step consists in looking for the maximum of the derivative

10   for differences over 5 K. Lastly, the cluster border is set at the minimal temperature difference so that half this maximum is reached (yellow vertical line in Fig. 7). The sensitivity of this value was analysed and showed that a change of $\pm$ 20 % had a very limited impact on the size of the lower cluster. It did not have a significant effect on the correlation of the resulting cloud mask with SYNOP observations either.

Due to the daily temperature cycle, days and nights are clustered separately to ensure that accurate lower cluster limits are

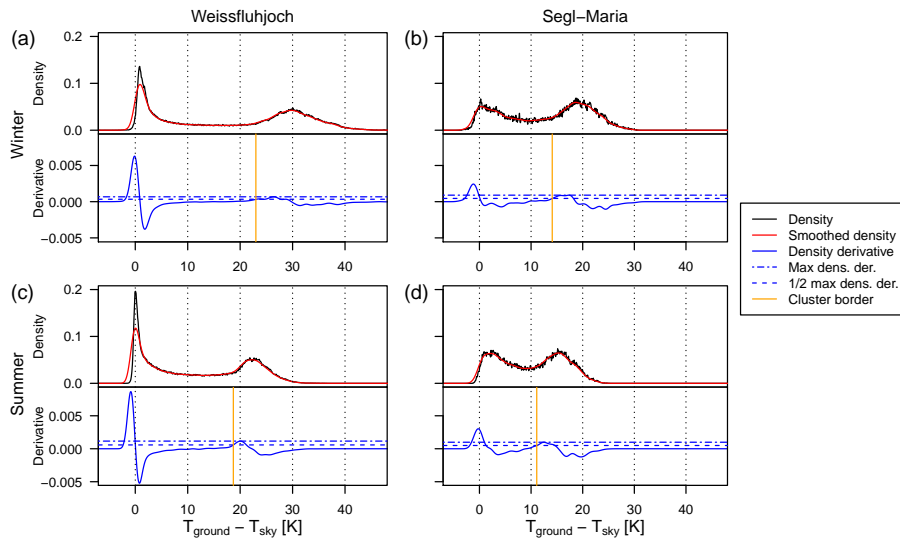15   obtained. Local sunrise and sunset times are used as time limits.

10

Figure 7. Detection of the longwave lower cluster on daytime data, at two different stations (left column, Weissfluhjoch; right column, Segl-Maria, one year of measurements), for winter (first row) and summer (second row) seasons.

Different applications of this method are shown in Fig. 7, for daytime conditions in winter and summer. One station with a long data record (Weissfluhjoch, 16 years) is compared to another one with a very short record (Segl-Maria, one year). As can be seen, the main advantage of detecting the cluster's border as a strong density increase is the excellent adaptability to different amounts of data as well as to different cluster shapes.

5   After this clustering step, two other criteria are combined to discriminate partially cloudy conditions from clear-sky ones (Fig. 8). The stability of the longwave measurements over the preceding hour is used as a sign of partial cloud cover, as in Dürr and Philipona (2004). However, a cloud is detected only if this criterion reaches a given threshold at the same time as the difference between estimated and measured shortwave radiation exceeds another threshold. Exploration of the parameter space in 2D has shown that this second criterion improves the classification, and that the threshold values are not particularly

10   sensitive. The stability of the longwave measurements over the preceding hour is computed as the root-mean-square deviation between the values and a linear fit applied to them (the threshold in the algorithm is set to $1.75 \ \mathrm{Wm^{-2}}$).

The shortwave criterion, C, is defined as a weighted sum of relative differences between the measured and estimated global radiation over the preceding hour (the threshold is set to 0.15 and is dimensionless). The weights are larger close to the time of interest t:

15
$$C = \frac{1}{28} \sum_{i=0}^{60} \frac{(70-i)}{10} \cdot \left| \frac{S_{\mathrm{e},t-i} - S_{\mathrm{m},t-i}}{S_{\mathrm{e},t-i}} \right|, \tag{2}$$

where i is a time index varying between 0 and 60 minutes by steps of 10 minutes, and $S_{\mathrm{m},t}$ and $S_{\mathrm{e},t}$ are respectively the measured and estimated global radiation, in $\mathrm{Wm^{-2}}$, at time t.
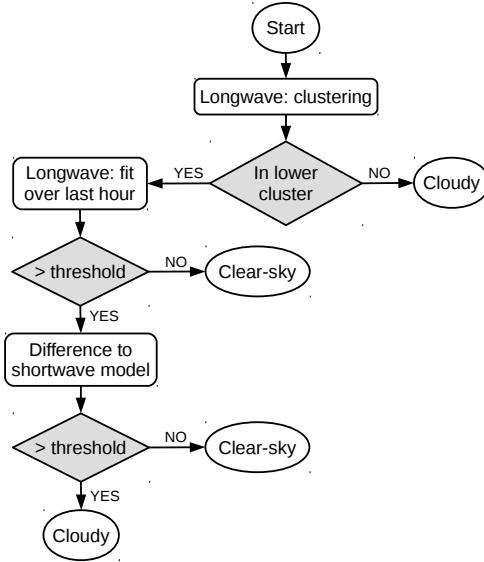
11

Figure 8. Cloud mask algorithm

The incoming global radiation $S_{e,t}$ is estimated using a simple model described in Sun et al. (2013), the model SW1 in their paper:

$$S_{e,t} = \tau \frac{S_0}{d_t^2} \cdot cos(\theta_t), \tag{3}$$

where τ is the atmospheric transmittance (dimensionless), S_0 the solar constant (1367 $\mathrm{Wm^{-2}}$), d_t the Earth-Sun distance (in

5   astronomical unit, AU) and θ_t the solar zenith angle (in radians) at time t. The particularity of this model is that the atmospheric transmittance τ is approximated as a linear function of the altitude, following Tasumi et al. (2000).

The shading effect of topography is taken into account due to its significant effect on radiation in mountainous areas (Lai et al., 2010). The shading angle H is defined as the minimal elevation above horizon required to see the sky above the sur-roundings. When the sun is at a given azimuth ϕ, if its elevation is below $H(\phi)$ then the estimated radiation is set to zero. The

10   shading angles were computed at each station using ASTER GDEM, taking into account surroundings up to a distance of 0.5 lat/lon degrees (55km/38km at 46°N), with a resolution of approximately 1 arc-second (15m/10m at 46°N).

3.4   Results

The obtained cloud mask was validated against SYNOP observations, with a time difference of at most 10 minutes. The percentages of misclassified clouds per okta is shown in Fig. 9. The largest source of error comes from the transformation

15   of the SYNOP observation into a binary threshold: it is difficult for the radiation cloud mask algorithm to follow this strict threshold when the distinction between 3 and 4 oktas is quite subjective. The cloud mask is hence accurate 85.4 % of the time, and this value reaches 90.3 % if both clear and cloudy classifications are allowed for 3- and 4-okta observations. With this
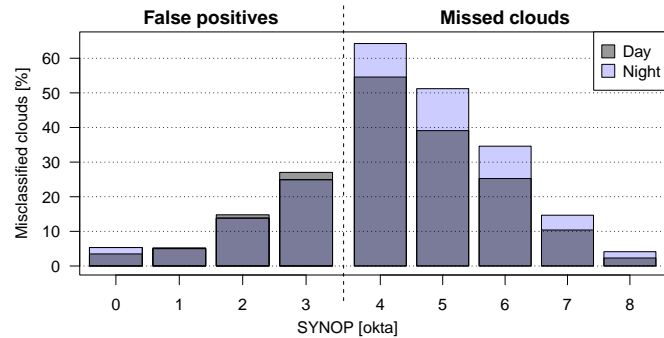
Figure 9. Distribution of the ground-based cloud mask errors as a function of SYNOP observations at 21 stations. The vertical dashed line represents the binary threshold applied to the SYNOP observations.

1-okta difference allowed, the probability of correctly detecting clouds is of 87.6 % and the probability of false detections of 5.6 %. This is consistent with Fig. 9, because more clear (0-1 okta) and cloudy (7-8 okta) conditions are recorded than partial ones. A bias of 0.913 oktas is present, confirming a tendency to miss some clouds. Thin and high clouds cause only minor perturbations in the radiation measurements compared to the clear sky conditions, and for this reason are more likely to be

5   missed. A larger amount of clouds are missed at night due to the lack of shortwave information. On the contrary, the negligible difference between false positives between day and night shows that a sparse cloud cover missed by the radiation instruments at night is most likely missed also by the human observer. The results' consistency is good among the different stations (the averaged accuracy is $91 \pm 2\%$), the lowest accuracy being at the Jungfraujoch (86 %), which is on a mountain pass where clouds can be observed below the observatory.

10   Even though the accuracy of the cloud mask presented here is limited for partially cloudy cases, these results are of great value for validation when a stable long-term reference is needed, such as in the validation of long-term satellite products. The results further suggest that this method could potentially be used outside the geographical area evaluated here, as the clustering method should adapt automatically to different climatic conditions.

4   Automated detection of false clouds

15   In this last section, a model is trained to automatically detect false positives in the satellite datasets. Using the radiation cloud mask as reference, this model combines several variables retrieved from satellite-measured radiances with information about the topography and time of the retrieval. The possibility of using the model at other times than those used as training is considered, and the model is applied to long satellite time series. Similarly, its ability to extrapolate to other locations than where it was trained is evaluated and maps of its effects are discussed.

4.1 Methods

A decision tree was trained to automate the identification of false clouds in the satellite datasets. The model's inputs are the five variables retrieved from the satellite radiances by the CC4CL algorithm (cloud phase, cloud optical thickness, cloud top pressure, cloud effective radius and surface temperature), as well as the ground altitude, the standard deviation of the surrounding ground altitudes, and a time variable. Time is represented as a sinusoidal function with a period of one year, peaking on the 15th of January (+1) and on the 15th of July (-1). The standard deviation of the surroundings is computed within a radius of 3 km on the 30-metre GDEM. Using these variables, the model predicts if the sky actually contains a cloud or not. The radiation cloud mask defined in Section 3 is used as reference for training. The training is done by 10-fold cross-validation with random sampling, using recursive partitioning as presented in Breiman (1984). Testing metrics are computed over the ten models obtained, and only the best one is then validated against SYNOP observations. After this validation, the structure of the model is discussed and some groups of points are defined. Focusing on these groups allows analysing the whole dimension space without considering each cloud property or each point one by one. The performance of the model is tested on each of these groups, and this permits the identification of some potential weaknesses.

Once validated, the decision tree is applied to the two satellite datasets presented at the beginning of this study. First, the effect of the model on times series of cloud properties is discussed. Then, leave-one-out validation is done to assess if the model can be applied at locations where it was not trained, and what kind of results can be expected in these circumstances. Leave-one-out validation consists in training several models, each with a training set composed of all but one station. Testing is done on this last station, and all the testing results are regrouped. Important information about the model weaknesses can be deduced from where the model had difficulties to adapt without training. It provides an overall idea about how the model will perform at locations where no reference data is available. Once this is done, the model is applied to a larger geographical area and the results are discussed as another insight on the model's strengths and weaknesses.

4.2 Analysis and validation of the model

The model obtained at the end of the training process is a large decision tree drawn in Fig. 10. After looking into the overall results, the groups of points circled in this figure are analysed more in detail.

Overall, the test metrics give a probability of 82.6 % of detecting false positives, and of 10.9 % of false detections. They are computed using the radiation cloud mask as reference, and averaged over the 10 tests of the cross-validation. When validated against SYNOP observations, results show that in winter above elevated areas, where most of the satellite false cloud detections happen, 73 ± 12 % of errors are identified (Table 1). The amount of missing clouds in these conditions is increased by 10 ± 4 %, whereas lower values are found in all other conditions. In summer, around 45 % of the overestimations are detected, with quite large differences between the stations, but with no significant link to the station's altitude. Globally, 62 ± 13 % of the cloud mask overestimations are detected, reducing the systematic false positive error from 14.4 ± 15.5 to 4.3 ± 2.8 % but increasing the missed clouds from 8.7 ± 3.5 to 15.6 ± 2.1 %. Although it might seem like this proposed correction only shifts the problem (from false clouds to missing clouds), it is not the case: the reduction of false positives is associated with a reduction of their
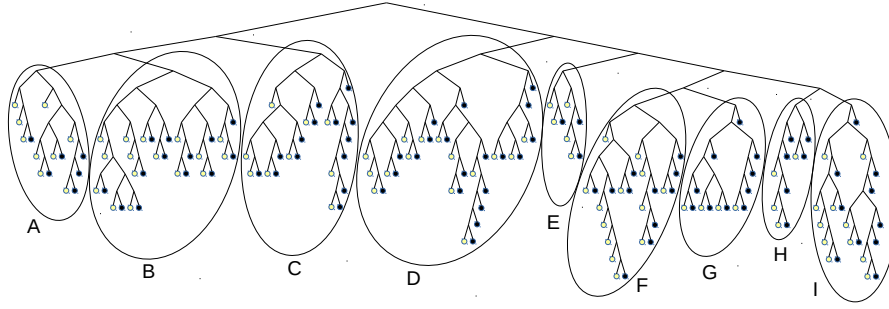
Figure 10. Structure of the model. Small circles correspond to the tree final nodes (also called leaves): light ones are classified as clear-sky, dark ones as cloudy. The parts circled and labelled with letters correspond to the groups of points defined in Table 2.

Table 1. Evaluation of the model's effects on MODIS dataset using SYNOP data as reference, at 20 SYNOP locations (7 above 1000m, 13 below; 4 stations with limited overlap between SYNOP and the ground-based radiation measurements were excluded). The two left columns contain the percentage of false positives in the satellite data that were correctly identified by the model. The two right ones contain the percentage of clouds identified in the satellite data which are considered false by the model, even though they are actual clouds according to SYNOP observations with the binary threshold applied.

	False positives correctly identified by the model [%]		Clouds wrongly identified by the model [%]	
	Winter	Summer	Winter	Summer
Above 1000m	73 ± 12	43 ± 24	10 ± 4	5 ± 3
Below 1000m	33 ± 24	47 ± 17	3 ± 3	5 ± 5

uncertainty (± 15.5 to ± 2.8). This means that the distribution of false positives is more homogeneous than before, and so, that the difference between high areas and lower ones has been reduced. Moreover, the increase ($+7$ %) of missed clouds is global, and does not correspond to a simple shift of the problem in elevated areas.

As proposed in Fig. 10, groups of points can be delineated in the tree and are characterised by the criteria detailed in Table 2. All of these groups are separated in subgroups that are not described here. As can be seen in the table, the cloud optical thickness (COT) is one of the most important variables in this model. Groups A and B, characterised by a small COT and which contain a large amount of well-classified points, most likely also contain a non-negligible amount of cirrus clouds, too thin to be seen by the reference cloud mask produced in this study. Group D is the only one containing only clouds located above mountains, and its high detection percentage confirms the efficiency of the model. Groups C, G, H, I are all characterised by low model performance. Group C can be understood as a small group of points scattered in the dimension space and which did not trigger a particular response of the model. The others are mainly composed of large COT, and group G probably corresponds to liquid phase clouds (CTP under 627 hPa and CER under 22 μm).

Table 2. Main branches of the tree. The letters in the first column correspond to the groups circled in Fig. 10. The second column states the amount of false positives (FP) in the satellite data falling into each branch, the third one how many of them were correctly identified by the model (IFP: Identified False Positives). The remaining columns describe the parameters and thresholds leading to each branch. COT: cloud optical thickness, CTP: cloud top pressure, CER: cloud effective radius.

Group	FP [%]	IFP [%]	Criteria			
A	10.5	87	$COT < 1.47$	time: not in winter (between mid-March and mid-November)		
B	13.0	73	$COT < 1.47$	time: in winter (between mid-November and mid-March)		
C	6.5	37	$1.47 \leq COT < 2.36$			
D	15.1	80	$2.36 \leq COT$	ground altitude ≥ 2988 m		
E	3.9	92	$2.36 \leq COT$	ground altitude < 2988 m	$CTP < 215$ hPa	
F	9.2	82	$2.36 \leq COT$	ground altitude < 2988 m	$627 \leq CTP$	$CER \geq 22$ μm
G	17.8	12	$2.36 \leq COT$	ground altitude < 2988 m	$627 \leq CTP$	$CER < 22$ μm
H	4.5	18	$2.36 \leq COT < 4.03$	ground altitude < 2988 m	$215 \leq CTP < 627$ hPa	
I	19.4	10	$4.03 \leq COT$	ground altitude < 2988 m	$215 \leq CTP < 627$ hPa	

As can be observed, groups of points that seem related (for instance, F and G) can be understood very differently by the model, which suggests that a more complex model could be necessary to catch subtle differences between false and real clouds, and improve the results.

4.3 Result of filtering the satellite dataset using the decision tree model

5 Having looked at the limitations of the model and at the expected results, the decision tree was then applied to the satellite-derived cloud property time series. The pixels corresponding to 9 stations above 1000m were extracted from the satellite dataset, and false clouds were detected and removed using the decision tree. The main cloud properties were observed before and after removal of these false positives, and are averaged per year and per month in Fig. 11. Although the model is trained on the MODIS-Aqua dataset only (2003-2014), a temporal extrapolation is attempted to the whole NOAA AVHRR-PM time

10 series (1982-2014).

After removal of the points identified by the model as likely not to be clouds, the cloud fractional cover (CFC) is lower. As expected, the points removed were more in winter than in summer, at higher altitudes, with larger optical thickness and smaller effective radius. This is highly consistent with the changes observed when removing from MODIS-Aqua dataset the clouds not observed by a human observer (Fig. 5). The difference between MODIS-Aqua and the MODIS-Aqua corrected time

15 series seems constant over time, and suggests that the effects of the model are temporally consistent. Over the years 2003-2014 the two satellite datasets agree very well, except for a small offset caused by the difference of spatial resolutions. Since the AVHRR series used here is not homogenized regarding e.g. drifts in overpass time between different NOAA satellites (Stengel et al., 2017a), its behaviour is not stable over time. This can be seen over the years 1982-2002, near the end of each NOAA
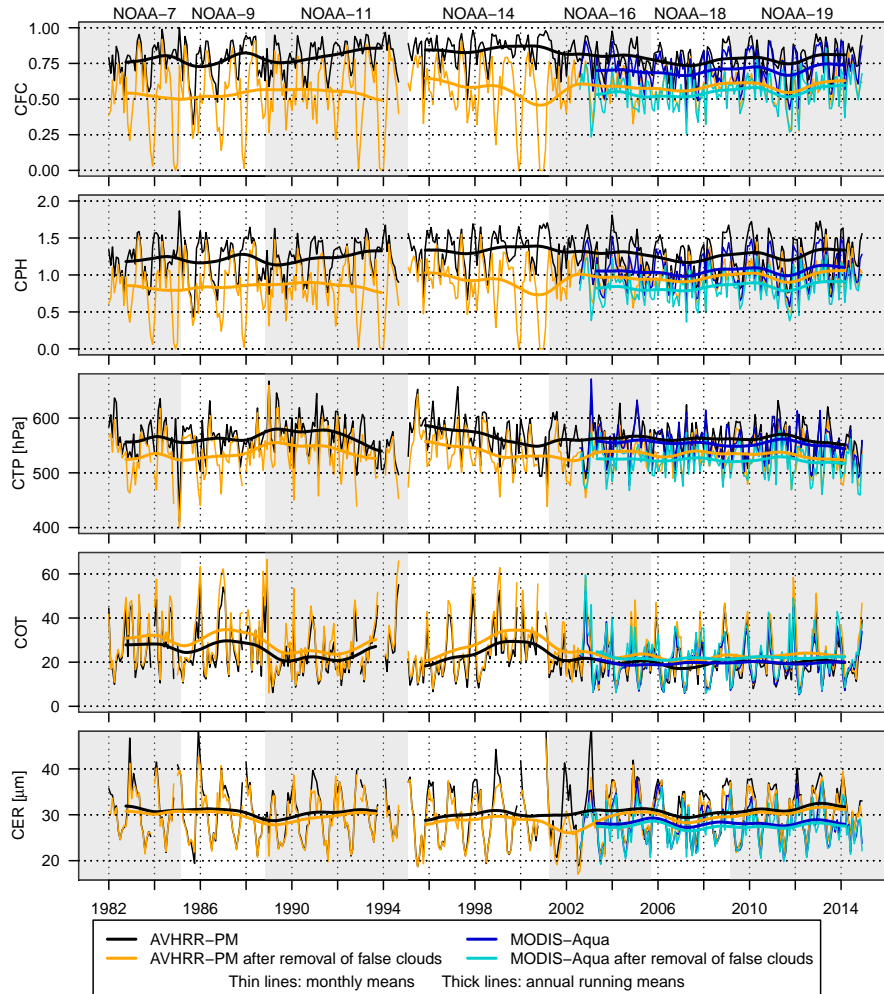
Figure 11. Time series of monthly means (thin lines) and annual moving averages (thick lines) of cloud properties, before and after removing points flagged by the model as potential false positives. 9 SYNOP stations located above 1000m are averaged together. CFC stands for cloud fractional cover, CPH for cloud phase (0: no cloud, 1: liquid phase, 2: ice phase), CTP for cloud top pressure, COT for cloud optical thickness and CER for cloud effective radius.

satellite, where values diverge progressively from their average. Some of these values are not expected by the model and tend to be removed, causing very low CFC values for several winters (at the end of 1983, 1984, 1987, etc.). As the satellites were drifting in time (up to 3h30 for NOAA 11), it suggests the need to first correct the cloud properties for the cloud diurnal cycle before applying the decision tree correction.

5   When compared to the latitude-weighted 60°S-60°N time series in Stengel et al. (2017a), the time series in Fig. 11 have wider seasonal amplitudes. The satellite's drifting in time also has a larger impact on the values. Both are related to the size of the areas over which the data are averaged. The proportion of cloud ice particles is significantly higher in the time series
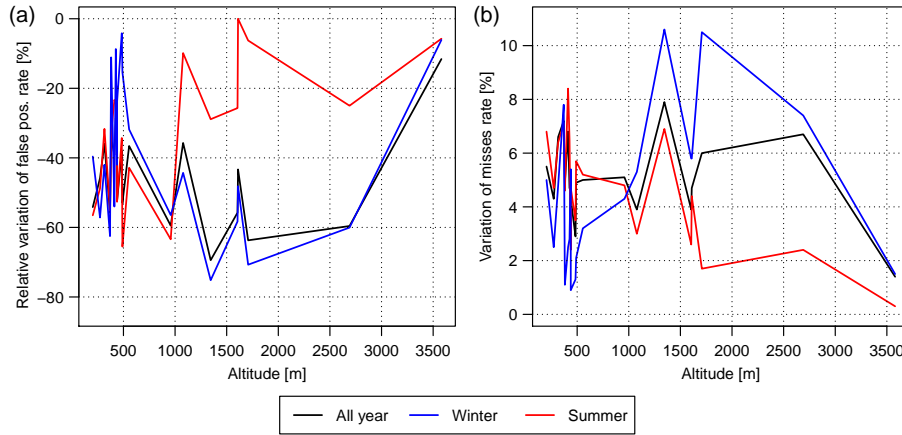
Figure 12. For each SYNOP station, a model was trained on all stations except one (leave-one-out validation). The figure shows the effect each model had on the rates of false positives (a, relative percentages) and missing clouds (b, absolute percentages) at the station left out, using SYNOP observations as reference.

in Switzerland than in Stengel et al. (2017a), even in low areas (results not shown), and after applying the model. Similarly, the cloud optical thickness is approximately twice as large in the time series presented here as in Stengel et al. (2017a). The cloud effective radius decrease from mid-2001 to mid-2003 is due to the change of channel on NOAA-16 (Heidinger et al., 2014), and can be observed in Stengel et al. (2017a) as an increase of effective radius. The channel 3.7 μm was switched to
5 1.6 μm, which seems to trigger the model. On this same property, a bias can be observed on values retrieved from NOAA-19, which seem to have an increasing difference with MODIS-Aqua. This can also be seen in Stengel et al. (2017a) and might be an instrumental bias.

4.4 Leave-one-out validation

The leave-one-out validation results in Fig. 12 suggest that the model can reliably be generalized in space, especially for
10 elevated areas in winter. The highest station of the dataset (Jungfraujoch) is an extreme case in this dataset, and cannot be well understood by the model if it is not part of the training set. Although good, the performance above elevated areas is lower in this validation than the values obtained previously on a slightly larger dataset (Table 1, errors correctly identified above 1000m). This suggests that increasing the amount of stations would be beneficial. However, even without increasing the number of stations, significant results (more than 50 % of the satellite cloud mask overestimations identified) can still be expected.
15   In this Figure 12, one can also observe that the detection of false positives in the satellite data is less efficient above elevated areas in summer, whereas in lower areas there is no significant seasonal difference. This might be a sign that seasonal differences in mountains are not fully understood by the model, probably due to the lower amount of stations above 1000m than below. As winters contain a much larger amount of false positives than summers, false positives in summer in high altitudes

end up being poorly represented in the dataset. Using a probabilistic approach taking into account the different amount of points in each condition might help reduce the model's skewness in favour of the detection of the most recurring problems.

No link seems to exist between the ability of the model to generalize to a station and the complexity of the station's surrounding, suggesting that the model already gets the most out of this variable. For stations below 1000m, a moderate negative correlation (-0.46) was found between the average relative increase of missing clouds caused by the model and the distance between a station and the center of its corresponding satellite pixel. A similar correlation (-0.43) was observed between this distance and the ability of the model to detect false positives in winter. This suggests that lower performance is partially caused by a spatial offset between the satellite viewing scene and the ground-based one. A solution out of the scope of this study would be to look more in detail into the satellite viewing geometry of the comparison scenes, and maybe to combine several satellite pixels in a weighted mean for comparison with a ground-based station.

4.5 Larger scale model application

Lastly, the model was applied on a large area and maps of the effect on the cloud coverage were produced (Fig. 13). They confirm that even at locations outside the training data, the model reduces cloud occurrences to more reasonable values above elevated areas, especially in winter (Fig. 13a). The systematic removal of 7 percent of the clouds (identified as false positives even though they were most likely real clouds) is not restricted to a specific area.

With a training set made of stations located only in Switzerland, the results appear very consistent above land also outside this area. Considering the model output over a wider area however illustrates its limitations, mainly over sea and lakes in every season apart from winter. Especially in summer, clouds are detected as false positives over water bodies, as their surface temperature is lower than that of the surrounding land. For instance, a blue spot can be seen in the Po valley of northern Italy (approx. 45.2 °N, 8.5 °E), where rice cultures are flooded during summer months, which significantly lowers the surface temperature. This confirms the importance that the model gives to the surface temperature, and suggests that either the model should be applied only over land, or it should be aware of the land/sea difference (for instance, adding a land/sea mask would be an easy step, but finding radiation measurements above sea for training might be difficult).

As applying a decision tree on data is a very quick process, this model is a simple solution to remove a significant amount of issues over elevated areas, for the reasonable cost of decreasing slightly and homogeneously the amount of clouds.

5 Conclusions

Two satellite datasets of ESA's CCI on clouds were seen to overestimate the cloud cover above elevated areas. MODIS-Aqua and AVHRR-PM can contain up to 54 % of false cloud detections in winter in mountainous areas (above ground with an elevation higher than 1000m). These cloud mask errors also have an important impact on the cloud properties, as retrievals on missing clouds often have unexpected values. Identifying them prior to any detailed analysis is a necessary step.

Using longwave and shortwave radiation measurements at 41 stations in Switzerland, a binary cloud mask was defined. It is tailored to each station and each season thanks to a simple automated clustering of the longwave data. Shortwave data and
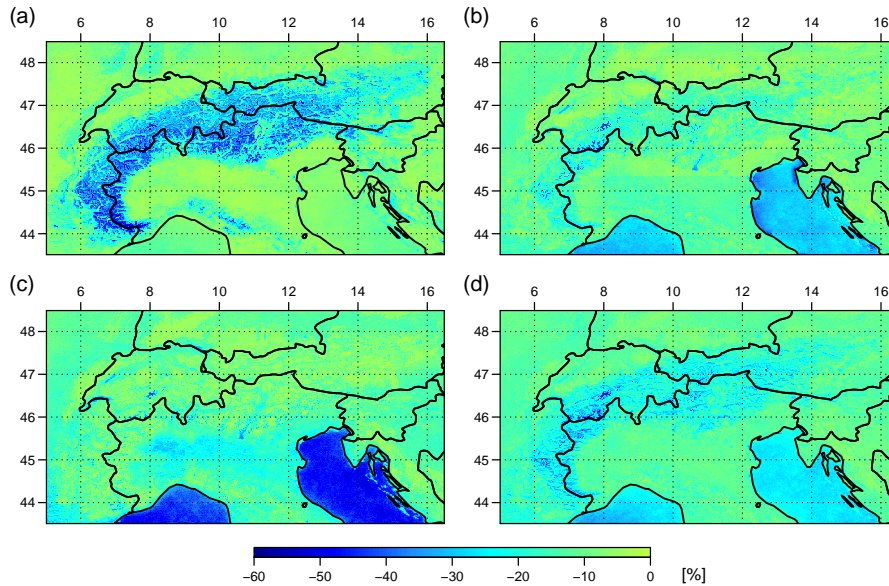
Figure 13. Effect of the model on cloud occurrences, in percent relative to the initial cloud occurrences. The results are averaged over MODIS-Aqua dataset (2003-2014) by season: winter (a), spring (b), summer (c) and autumn (d). The seasons are defined as Dec.Jan.Feb., Mar.Apr.May, JuneJulyAug., Sep.Oct.Nov.

a second longwave criterion are then used to provide more insight in partially cloudy cases. Validation against SYNOP shows that the model has a probability of 87.6 % of detecting cloudy skies using this combination of ground-based information, and a probability of 5.6 % of false detections.

This ground-based cloud mask was then used as reference to train a model for the detection of false clouds in the satellite
5   datasets. The model's input contains variables such as the satellite-retrieved cloud properties, ground and time information. In the Swiss Alpine region, the use of the decision tree model as a quality filter permitted the rejection of 62 % of the false cloud detections in the satellite cloud property dataset, with the limitation of causing the removal of 7 % of real clouds in the process. This made a significant improvement to the quality of the satellite cloud property data set over this area. These results are interesting for any application where one can afford to reduce the amount of data in order to increase its quality.
10   Improved results might be obtained by using a probabilistic approach, likely to allow under-represented categories to be better understood. A higher number of elevated stations could also be beneficial. Expanding the study area to other latitudes using either already computed cloud masks, or data from the worldwide Baseline Surface Radiation Network (BSRN Ohmura et al., 1998) for instance, would be an expected follow-up.

Considering how time- and resources-consuming is the computation of large satellite datasets, fast post-processing algo-
15   rithms such as the one proposed in this study are likely to be interesting solutions as more and more data are available.

20

Moreover, as demonstrated here, having several datasets produced by the same retrieval algorithm is a great asset as it allows them to be post-processed in the same manner.

Appendix A: List of ground-based stations

Table A1. Location and data coverage of the 41 ground-based stations used in this study. The length of overlap with MODIS is not specified when the whole record overlaps temporally with the MODIS time range (2002-08-01 to 2014-12-31).

Location	Altitude [m]	Latitude [deg. N]	Longitude [deg. E]	Radiation			SYNOP		
				Start	End	Length [years] (MODIS overlap)	Start	End	Length [years] (MODIS overlap)
Aadorf	539	47.47987	8.90487	2006-10	✓	8.2	1980-01	2007-02	27.2 (4.6)
Aigle	381	46.32664	6.92442	2005-09	✓	9.3	1981-02	✓	33.9 (12.4)
Altdorf	438	46.88702	8.62180	2008-12	✓	6.1	1980-01	✓	35.0 (12.4)
Bad Ragaz	496	47.01662	9.50257	2012-02	✓	2.9	-	-	-
Basel	316	47.54103	7.58356	2009-12	✓	5.1	1980-01	✓	35.0 (12.4)
Bern	552	46.99074	7.46400	2009-09	✓	5.3	-	-	-
Chasseral	1599	47.13176	7.05439	2010-10	✓	4.2	-	-	-
Château-d'Oex	1029	46.47981	7.13964	2012-02	✓	2.9	1980-01	2011-08	31.7 (9.1)
Cimetta *	1670	46.20042	8.79164	1995-12	2010-12	15.1 (8.4)	-	-	-
Davos	1610	46.81297	9.84349	1999-01	✓	17.0 (13.4)	1980-01	2005-11	25.9 (3.3)
Einsiedeln	910	47.13304	8.75655	2012-03	✓	2.8	1980-01	2012-04	32.3 (9.7)
Elm	958	46.92375	9.17534	2011-04	✓	3.7	1980-01	✓	35.0 (12.4)
Engelberg	1035	46.82189	8.41044	2012-08	✓	2.4	-	-	-
Fahy	596	47.42382	6.94110	2009-11	✓	5.2	-	-	-
Genève-Cointrin	412	46.24751	6.12774	2012-05	✓	2.6	1980-01	✓	35.0 (12.4)
Glarus	516	47.03458	9.06690	2013-08	✓	1.4	-	-	-
Grächen	1605	46.19531	7.83682	2013-06	✓	1.6	1980-01	✓	35.0 (12.4)
Grimsel Hospiz	1980	46.57169	8.33325	2012-09	✓	2.3	-	-	-
Gütsch ob And.	2283	46.65244	8.61505	2005-09	✓	9.3	-	-	-
Jungfraujoch	3580	46.54745	7.98533	1999-01	✓	17.0 (13.4)	1980-01	✓	35.0 (12.4)
Koppigen	484	47.11884	7.60549	2012-01	✓	3.0	1980-01	✓	35.0 (12.4)
La Dôle	1669	46.42470	6.09948	2009-10	✓	5.2	-	-	-
Locarno *	370	46.17223	8.78750	1995-12	2010-12	15.1 (8.4)	1980-01	✓	35.0 (12.4)
Lugano	273	46.00423	8.96031	2012-12	✓	2.1	1980-01	✓	35.0 (12.4)
Luzern	454	47.03643	8.30096	2013-05	✓	1.7	-	-	-
Magadino	203	46.16003	8.93366	2006-02	✓	8.9	1980-01	2010-11	30.8 (12.4)
Napf	1403	47.00466	7.94004	2007-07	✓	7.5	-	-	-
Neuchâtel	485	47.00006	6.95329	2010-10	✓	4.2	-	-	-
Nyon	455	46.40105	6.22775	2005-10	2009-07	3.7	-	-	-
Payerne *	490	46.81158	6.94242	1995-01	2010-12	16.0 (8.4)	1980-01	✓	35.0 (12.4)
Plaffeien	1042	46.74766	7.26600	2005-08	2009-06	3.9	-	-	-
Poschiavo	1078	46.34664	10.06113	2008-01	✓	6.9	1980-01	✓	35.0 (12.4)
Ruenenberg	611	47.43456	7.87932	2013-12	✓	1.1	-	-	-
Samedan	1708	46.52640	9.87894	2012-12	✓	2.1	1980-01	✓	35.0 (12.4)
Schaffausen	438	47.68977	8.62006	2008-08	✓	6.4	2004-02	2013-05	9.2
Segl-Maria	1804	46.43233	9.76230	2014-03	✓	0.8	1980-01	2014-06	34.5 (11.9)
Stabio	353	45.84339	8.93238	2009-10	✓	5.2	-	-	-
Ulrichen	1345	46.50482	8.30814	2008-06	✓	6.6	1999-09	✓	15.3 (12.4)
Weissfluhjoch *	2690	46.83334	9.80638	1994-09	2010-12	16.3 (8.4)	1980-01	2008-06	28.5 (5.9)
Zürich Fluntern	555	47.37792	8.56572	2012-10	✓	2.2	1980-01	✓	35.0 (12.4)
Zürich Kloten	426	47.47961	8.53595	2010-03	✓	4.8	1980-01	✓	35.0 (12.4)

*: Radiation data from the ASRB network. If not specified, radiation data are from MeteoSwiss. All SYNOP observations are from MeteoSwiss.

✓: End date of the ground-based record is after the end of the satellite records (2014-12-31).

References

Barbaro, S., Cannata, G., Coppolino, S., Leone, C., and Sinagra, E.: Correlation between relative sunshine and state of the sky, Solar Energy, 26, 537–550, https://doi.org/10.1016/0038-092X(81)90166-3, 1981.

Barnes, W., Pagano, T., and Salomonson, V.: Prelaunch characteristics of the Moderate Resolution Imaging Spectroradiometer (MODIS) on EOS-AM1, IEEE Transactions on Geoscience and Remote Sensing, 36, 1088–1100, https://doi.org/10.1109/36.700993, 1998.

Bojanowski, J., Stöckli, R., Tetzlaff, A., and Kunz, H.: The Impact of Time Difference between Satellite Overpass and Ground Observation on Cloud Cover Performance Statistics, Remote Sensing, 6, 12 866–12 884, https://doi.org/10.3390/rs61212866, 2014.

Breiman, L.: Classification and regression trees, Chapman & Hall/CRC, New York, N.Y., http://lib.myilibrary.com?id=1043565, oCLC: 1022760542, 1984.

Cracknell, A. P.: The advanced very high resolution radiometer (AVHRR), Taylor & Francis, London ; Bristol, PA, 1997.

Davies, R., Jovanovic, V. M., and Moroney, C. M.: Cloud heights measured by MISR from 2000 to 2015, Journal of Geophysical Research: Atmospheres, 122, 3975–3986, https://doi.org/10.1002/2017JD026456, 2017.

Dee, D. P., Uppala, S. M., Simmons, A. J., Berrisford, P., Poli, P., Kobayashi, S., Andrae, U., Balmaseda, M. A., Balsamo, G., Bauer, P., Bechtold, P., Beljaars, A. C. M., van de Berg, L., Bidlot, J., Bormann, N., Delsol, C., Dragani, R., Fuentes, M., Geer, A. J., Haimberger, L., Healy, S. B., Hersbach, H., Hólm, E. V., Isaksen, L., Kållberg, P., Köhler, M., Matricardi, M., McNally, A. P., Monge-Sanz, B. M., Morcrette, J.-J., Park, B.-K., Peubey, C., de Rosnay, P., Tavolato, C., Thépaut, J.-N., and Vitart, F.: The ERA-Interim reanalysis: configuration and performance of the data assimilation system, Quarterly Journal of the Royal Meteorological Society, 137, 553–597, https://doi.org/10.1002/qj.828, 2011.

Dupont, J.-C., Haeffelin, M., and Long, C. N.: Evaluation of cloudless-sky periods detected by shortwave and longwave algorithms using lidar measurements, Geophysical Research Letters, 35, https://doi.org/10.1029/2008GL033658, 2008.

Dürr, B. and Philipona, R.: Automatic cloud amount detection by surface longwave downward radiation measurements, Journal of Geophysical Research, 109, https://doi.org/10.1029/2003JD004182, 2004.

Fontana, F., Lugrin, D., Seiz, G., Meier, M., and Foppa, N.: Intercomparison of satellite- and ground-based cloud fraction over Switzerland (2000–2012), Atmospheric Research, 128, 1–12, https://doi.org/10.1016/j.atmosres.2013.01.013, 2013.

Heidinger, A. K., Foster, M. J., Walther, A., and Zhao, X. T.: The Pathfinder Atmospheres–Extended AVHRR Climate Dataset, Bulletin of the American Meteorological Society, 95, 909–922, https://doi.org/10.1175/BAMS-D-12-00246.1, 2014.

Herrmann, E., Weingartner, E., Henne, S., Vuilleumier, L., Bukowiecki, N., Steinbacher, M., Conen, F., Collaud Coen, M., Hammer, E., Jurányi, Z., Baltensperger, U., and Gysel, M.: Analysis of long-term aerosol size distribution data from Jungfraujoch with emphasis on free tropospheric conditions, cloud influence, and air mass transport, Journal of Geophysical Research: Atmospheres, 120, 9459–9480, https://doi.org/10.1002/2015JD023660, 2015.

Hollmann, R., Merchant, C. J., Saunders, R., Downy, C., Buchwitz, M., Cazenave, A., Chuvieco, E., Defourny, P., de Leeuw, G., Forsberg, R., Holzer-Popp, T., Paul, F., Sandven, S., Sathyendranath, S., van Roozendael, M., and Wagner, W.: The ESA Climate Change Initiative: Satellite Data Records for Essential Climate Variables, Bulletin of the American Meteorological Society, 94, 1541–1552, https://doi.org/10.1175/BAMS-D-11-00254.1, 2013.

Karlsson, K.-G.: A 10 year cloud climatology over Scandinavia derived from NOAA Advanced Very High Resolution Radiometer imagery, International Journal of Climatology, 23, 1023–1044, https://doi.org/10.1002/joc.916, 2003.

Lai, Y.-J., Chou, M.-D., and Lin, P.-H.: Parameterization of topographic effect on surface solar radiation, Journal of Geophysical Research, 115, https://doi.org/10.1029/2009JD012305, 2010.

Long, C. N., Ackerman, T. P., Gaustad, K. L., and Cole, J. N. S.: Estimation of fractional sky cover from broadband shortwave radiometer measurements, Journal of Geophysical Research, 111, https://doi.org/10.1029/2005JD006475, 2006.

5 Malberg, H.: Comparison of Mean Cloud Cover Obtained By Satellite Photographs and Ground-Based Observations Over Europe and the Atlantic, Monthly Weather Review, 101, 893–897, https://doi.org/10.1175/1520-0493(1973)101<0893:COMCCO>2.3.CO;2, 1973.

Marty, C., Philipona, R., Fröhlich, C., and Ohmura, A.: Altitude dependence of surface radiation fluxes and cloud forcing in the alps: results from the alpine surface radiation budget network, Theoretical and Applied Climatology, 72, 137–155, https://doi.org/10.1007/s007040200019, 2002.

10 Martínez-Chico, M., Batlles, F., and Bosch, J.: Cloud classification in a mediterranean location using radiation data and sky images, Energy, 36, 4055–4062, https://doi.org/10.1016/j.energy.2011.04.043, 2011.

McGarragh, G. R., Poulsen, C. A., Thomas, G. E., Povey, A. C., Sus, O., Stapelberg, S., Schlundt, C., Proud, S., Christensen, M. W., Stengel, M., Hollmann, R., and Grainger, R. G.: The Community Cloud retrieval for CLimate (CC4CL). Part 2: The optimal estimation approach, Atmospheric Measurement Techniques, 11, 3397–3431, https://doi.org/10.5194/amt-11-3397-2018, https://www.atmos-meas-tech.net/11/

15 3397/2018/, 2018.

Mittermaier, M.: A critical assessment of surface cloud observations and their use for verifying cloud forecasts, Quarterly Journal of the Royal Meteorological Society, 138, 1794–1807, https://doi.org/10.1002/qj.1918, 2012.

Musial, J. P., Hüsler, F., Sütterlin, M., Neuhaus, C., and Wunderle, S.: Probabilistic approach to cloud and snow detection on Advanced Very High Resolution Radiometer (AVHRR) imagery, Atmospheric Measurement Techniques, 7, 799–822, https://doi.org/10.5194/amt-7-799-

20 2014, 2014.

Norris, J. R., Allen, R. J., Evan, A. T., Zelinka, M. D., O'Dell, C. W., and Klein, S. A.: Evidence for climate change in the satellite cloud record, Nature, 536, 72–75, https://doi.org/10.1038/nature18273, 2016.

Ohmura, A., Gilgen, H., Hegner, H., Müller, G., Wild, M., Dutton, E. G., Forgan, B., Fröhlich, C., Philipona, R., Heimo, A., König-Langlo, G., McArthur, B., Pinker, R., Whitlock, C. H., and Dehne, K.: Baseline Surface Radiation Network (BSRN/WCRP): New Preci-

25 sion Radiometry for Climate Research, Bulletin of the American Meteorological Society, 79, 2115–2136, https://doi.org/10.1175/1520-0477(1998)079<2115:BSRNBW>2.0.CO;2, 1998.

Pagès, D., Calbó, J., and González, J. A.: Using routine meteorological data to derive sky conditions, Annales Geophysicae, 21, 649–654, https://doi.org/10.5194/angeo-21-649-2003, 2003.

Pavolonis, M. J. and Heidinger, A. K.: Daytime Cloud Overlap Detection from AVHRR and VIIRS, Journal of Applied Meteorology, 43,

30 762–778, https://doi.org/10.1175/2099.1, http://journals.ametsoc.org/doi/abs/10.1175/2099.1, 2004.

Pavolonis, M. J., Heidinger, A. K., and Uttal, T.: Daytime Global Cloud Typing from AVHRR and VIIRS: Algorithm Description, Validation, and Comparisons, Journal of Applied Meteorology, 44, 804–826, https://doi.org/10.1175/JAM2236.1, http://journals.ametsoc.org/doi/abs/10.1175/JAM2236.1, 2005.

Pepin, N., Bradley, R. S., Diaz, H. F., Baraer, M., Caceres, E. B., Forsythe, N., Fowler, H., Greenwood, G., Hashmi, M. Z., Liu,

35 X. D., Miller, J. R., Ning, L., Ohmura, A., Palazzi, E., Rangwala, I., Schöner, W., Severskiy, I., Shahgedanova, M., Wang, M. B., Williamson, S. N., and Yang, D. Q.: Elevation-dependent warming in mountain regions of the world, Nature Climate Change, 5, 424–430, https://doi.org/10.1038/nclimate2563, 2015.

Quaas, J.: Approaches to Observe Anthropogenic Aerosol-Cloud Interactions, Current Climate Change Reports, 1, 297–304, https://doi.org/10.1007/s40641-015-0028-0, 2015.

Rangwala, I. and Miller, J. R.: Climate change in mountains: a review of elevation-dependent warming and its possible causes, Climatic Change, 114, 527–547, https://doi.org/10.1007/s10584-012-0419-3, 2012.

5   Rodgers, C. D.: Inverse methods for atmospheric sounding: theory and practice, no. 2 in Series on atmospheric oceanic and planetary physics, World Scientific, Singapore, reprinted edn., 2004.

Schaaf, C. B., Liu, J., Gao, F., and Strahler, A. H.: Aqua and Terra MODIS Albedo and Reflectance Anisotropy Products, in: Land Remote Sensing and Global Environmental Change, edited by Ramachandran, B., Justice, C. O., and Abrams, M. J., vol. 11, pp. 549–561, Springer New York, New York, NY, https://doi.org/10.1007/978-1-4419-6749-7_24, http://link.springer.com/10.1007/978-1-4419-6749-7_24,
10   2010.

Stapelberg, S., Stengel, M., Karlsson, K.-G., Meirink, J. F., Bojanowski, J., and Hollmann, R.: ESA Cloud_cci Product Validation and Intercomparison Report (PVIR), Tech. Rep. 4.1, http://www.esa-cloud-cci.org/?q=documentation, 2017.

Stengel, M., Mieruch, S., Jerg, M., Karlsson, K.-G., Scheirer, R., Maddux, B., Meirink, J., Poulsen, C., Siddans, R., Walther, A., and Hollmann, R.: The Clouds Climate Change Initiative: Assessment of state-of-the-art cloud property retrieval schemes applied to AVHRR
15   heritage measurements, Remote Sensing of Environment, 162, 363–379, https://doi.org/10.1016/j.rse.2013.10.035, 2015.

Stengel, M., Stapelberg, S., Sus, O., Schlundt, C., Poulsen, C., Thomas, G., Christensen, M., Carbajal Henken, C., Preusker, R., Fischer, J., Devasthale, A., Willén, U., Karlsson, K.-G., McGarragh, G. R., Proud, S., Povey, A. C., Grainger, D. G., Meirink, J. F., Feofilov, A., Bennartz, R., Bojanowski, J., and Hollmann, R.: Cloud property datasets retrieved from AVHRR, MODIS, AATSR and MERIS in the framework of the Cloud_cci project, Earth System Science Data Discussions, pp. 1–34, https://doi.org/10.5194/essd-2017-48, 2017a.

20   Stengel, M., Sus, O., Stapelberg, S., Schlundt, C., Poulsen, C., and Hollmann, R.: ESA Cloud_cci cloud property datasets retrieved from passive satellite sensors: AVHRR-PM L3C/L3U cloud products - Version 2.0, https://doi.org/10.5676/DWD/ESA_Cloud_cci/AVHRR-PM/V002, 2017b.

Stengel, M., Sus, O., Stapelberg, S., Schlundt, C., Poulsen, C., and Hollmann, R.: ESA Cloud_cci cloud property datasets retrieved from passive satellite sensors: MODIS-Aqua L3C/L3U cloud products - Version 2.0, https://doi.org/10.5676/DWD/ESA_Cloud_cci/MODIS-
25   Aqua/V002, 2017c.

Sun, Z., Gebremichael, M., Wang, Q., Wang, J., Sammis, T., and Nickless, A.: Evaluation of Clear-Sky Incoming Radiation Estimating Equations Typically Used in Remote Sensing Evapotranspiration Algorithms, Remote Sensing, 5, 4735–4752, https://doi.org/10.3390/rs5104735, 2013.

Sus, O., Stengel, M., Stapelberg, S., McGarragh, G., Poulsen, C., Povey, A. C., Schlundt, C., Thomas, G., Christensen, M., Proud, S.,
30   Jerg, M., Grainger, R., and Hollmann, R.: The Community Cloud retrieval for CLimate (CC4CL). Part 1: A framework applied to multiple satellite imaging sensors, Atmospheric Measurement Techniques, 11, 3373–3396, https://doi.org/10.5194/amt-11-3373-2018, https://www.atmos-meas-tech.net/11/3373/2018/, 2018.

Suter, S., Konzelmann, T., Mühlhäuser, C., Begert, M., and Heimo, A.: SwissMetNet - the new automatic meteorological network of Switzerland: transition from old to new network, data management and first results, Altis Park Hotel, Lisbon, 2006.

35   Tachikawa, T., Hato, M., Kaku, M., and Iwasaki, A.: Characteristics of ASTER GDEM version 2, pp. 3657–3660, IEEE, https://doi.org/10.1109/IGARSS.2011.6050017, 2011.

Tasumi, M., Allen, R., and Bastiaanssen, M.: The Theoretical Basis of SEBAL, Tech. rep., Idaho Department of Water Resources, 2000.

Trenberth, K. E.: An imperative for climate change planning: tracking Earth's global energy, Current Opinion in Environmental Sustainability, 1, 19–27, https://doi.org/10.1016/j.cosust.2009.06.001, 2009.

Viúdez-Mora, A., Calbó, J., González, J. A., and Jiménez, M. A.: Modeling atmospheric longwave radiation at the surface under cloudless skies, Journal of Geophysical Research, 114, https://doi.org/10.1029/2009JD011885, 2009.

5 Werkmeister, A., Lockhoff, M., Schrempf, M., Tohsing, K., Liley, B., and Seckmeyer, G.: Comparing satellite- to ground-based automated and manual cloud coverage observations – a case study, Atmospheric Measurement Techniques, 8, 2001–2015, https://doi.org/10.5194/amt-8-2001-2015, 2015.

Winker, D. M., Vaughan, M. A., Omar, A., Hu, Y., Powell, K. A., Liu, Z., Hunt, W. H., and Young, S. A.: Overview of the CALIPSO Mission and CALIOP Data Processing Algorithms, Journal of Atmospheric and Oceanic Technology, 26, 2310–2323,
10 https://doi.org/10.1175/2009JTECHA1281.1, http://journals.ametsoc.org/doi/abs/10.1175/2009JTECHA1281.1, 2009.